THE ASTROPHYSICAL JOURNAL, 493:L91–L94, 1998 February 1

SYNTHETIC IMAGES AND LONG-SLIT SPECTRA OF PROTOSTELLAR JETS

HSIEN SHANG AND FRANK H. SHU
Astronomy Department, University of California, Berkeley, CA 94720-3411
AND
ALFRED E. GLASSGOLD
Physics Department, New York University, New York, NY 10003
Received 1997 September 18; accepted 1997 November 20; published 1998 January 14

ABSTRACT

We construct synthetic images and long-slit spectra of protostellar jets modeled as steady state X-winds. Assuming uniform ionization fractions and electron temperatures, we calculate non-LTE level populations for five-level atoms. Synthetic images in the [S II] λ6716/λ6731 and [O I] λ6300/λ6364 lines have roughly the same surface brightness as observed jets if we ignore their knotty structure. Long-slit spectra taken with the slit placed along the central axis of the jet, or slightly displaced laterally from it, provide strong evidence in support of the X-wind theory. In both the models and the actual objects, wide line profiles, containing both large positive and negative velocities, are often seen at the base of the flow, indicative of a wide-angle wind. As one progresses up the length of the slit, the line profiles narrow to straddle the projected velocity of a highly collimated jet.

Subject headings: ISM: jets and outflows — line: profiles — stars: pre–main-sequence

1. INTRODUCTION

Herbig-Haro objects and their association with highly collimated outflows from young stellar objects (YSOs) are one of the most important observational discoveries in the field of star formation (Haro 1950; Herbig 1950; Bok 1978; Cudworth & Herbig 1979). The relationship between the jets that these objects trace (Mundt & Fried 1983; Reipurth & Heathcote 1991) and the bipolar molecular outflows of swept-up ambient gas around many YSOs has been a controversial subject since the latter were first discovered (Snell et al. 1980; Rodriguez, Ho, & Moran 1980; Bally & Lada 1983; Welch et al. 1985). At the heart of the controversy are the following questions. What provides the source of momentum, through shock waves or turbulent entrainment, for driving CO bipolar outflow? Is it the observed optical jet or a wide-angle wind whose densest central manifestation appears as a jet? (See the reviews of Bachiller 1996 and Cabrit, Raga, & Gueth 1997.)

Shu et al. (1991, hereafter SRLL) proposed a particularly simple description of the interaction of wide-angle winds with flattened molecular cloud cores. Among other desirable features, the model readily explains observed CO lobe shapes and the "Hubble law" of the dependence of the line-of-sight velocity $v_\parallel$ of swept-up gas with distance L along the bipolar flow axis. Masson & Chernin (1992) and Chernin & Masson (1995) argued that SRLL models contradict the observed distributions of (*a*) mass M with $v_\parallel$ and (*b*) momentum P contained in the swept-up gas as a function of L. These objections were answered by the calculations of Li & Shu (1996), who reexamined SRLL models in the particular case in which the X-wind (Shu et al. 1994) has the asymptotic characteristics described by Shu et al. (1995, hereafter SNOS) and in which the molecular cloud core is a magnetized singular isothermal toroid with a degree of flattening compatible with the measurements of Myers et al. (1991). For these physically motivated choices derived from a priori theoretical considerations, the SRLL prescription does indeed reproduce the observed distributions, $M(v_\parallel)$ and $P(L)$, with no adjustment of model parameters.

Nevertheless, it would be desirable to demonstrate the existence of a wide-angle wind in the data directly without having to infer its presence from interactions with the ambient matter. Shu & Shang (1997) suggested that differences in line-profile shapes at the base of the flow and in the jet proper, as determined from forbidden-line images in [S II] and [O I], could provide a discriminant between X-wind and pure-jet models. The present Letter provides a quantitative analysis of the efficacy of this test.

2. LEVEL POPULATIONS

At gas temperatures $T \sim 10^4$ K, probably produced by shock wave pulses emanating from the central source with a duty cycle $\sim 10^1$ yr (Raga 1995; Shu et al. 1997), it suffices to treat the excitation of the relevant outer electron configurations of S II and O I with a five-level atom (Mendoza 1983). The equations of statistical equilibrium for the densities n_j and n_k of atoms occupying the atomic levels j and k in an optically thin medium with electron density n_e read

$$\sum_{j>k} n_j A_{jk} + \sum_{j\neq k} n_j n_e C_{jk} = \sum_{j<k} n_k A_{kj} + \sum_{j\neq k} n_k n_e C_{kj}, \quad k = 1, 2, 3, 4, 5, \quad (1)$$

where we assume that excitation and de-excitation collisions are dominated by electrons. If we also sum over k, the summed left-hand side is equal to the summed right-hand side. This result holds because only four of the five equations are independent; the fifth equation is redundant because of number conservation:

$$\sum_{k=1}^{5} n_k = \text{constant} \equiv n_0. \quad (2)$$

In equation (1), collisional excitation rates for $k > j$ are related to de-excitation rates via the Boltzmann condition:

$$C_{jk} = \frac{g_k}{g_j} C_{kj} \exp(-E_{kj}/kT), \quad (3)$$

where T is the electron kinetic temperature and C_{kj} is only a

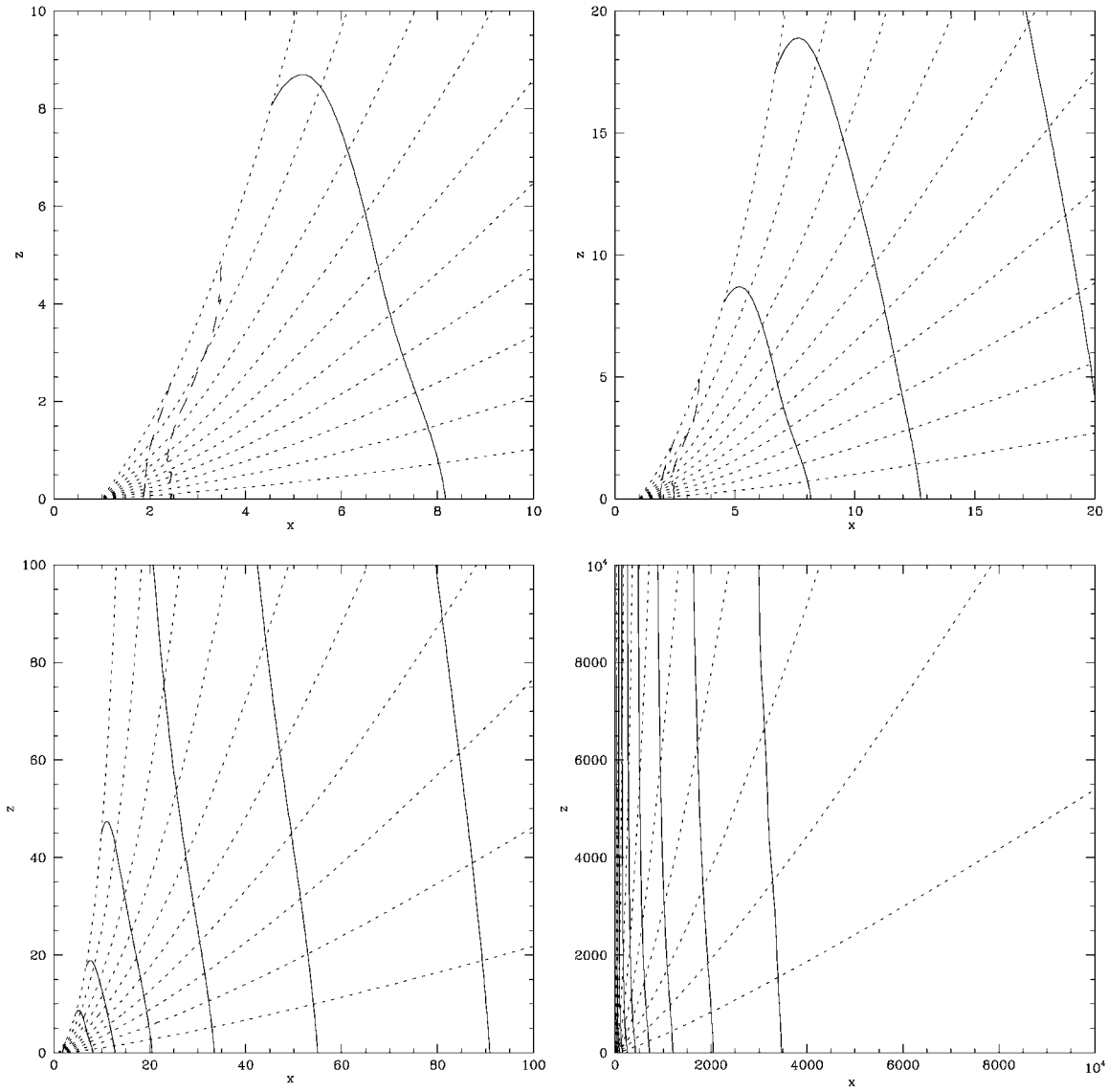

FIG. 1.—Isodensity contours (*solid curves*) and streamlines (*dotted curves*) for a cold X-wind. The units of length are R_X. Isodensity contours are spaced logarithmically in intervals of $\Delta \log_{10} \rho = 0.5$, and streamlines are spaced so that successive dotted lines contain an additional 10% of the total mass loss in the upper hemisphere of the flow. The loci of the Alfvén and fast surfaces are marked by dashed lines. The empty space inside the uppermost streamline, $\varpi \leq \varpi_1$, is filled with open field lines from the central star.

function of T. For given n_e , n_0, and T, equations (1) and (2) divided by n_0 can be solved as a linear matrix equation for the level population fraction $x_k \equiv n_k/n_0$, $k = 1, 2, 3, 4, 5$. For any $k = u$ and $j = l$, with $hc/\lambda_{ul} = E_{ul}$, we may then substitute the results into the computational method of the next section to compute spatially resolved line profiles. The displayed examples correspond to the choices: electron temperature $T =$ 8000 K and electron fraction $x_e \equiv mn_e/\rho = 0.1$, where ρ is the local mass density and $m = 2.2 \times 10^{-24}$ g cm^{-3} is the mean mass of the molecular, atomic, and ionic species in the X-wind. We adopt a number abundance for S II and O I relative to ρ/m equal to 1.6×10^{-5} and 8.5×10^{-4}, respectively. The relevant atomic data are all taken from Mendoza (1983).

3. COMPUTATIONAL METHOD FOR IMAGES AND SPECTRA

We divide space into cells of uniform volume $\Delta V' = \Delta x' \Delta y' \Delta z'$ in the observer's (x', y', z') coordinates. The observer lies at a great distance D from the source in the direction of the z' axis, which is tilted at an angle i with respect to the spin axis (z) of the source. The protostar is centered on the origin of the (x', y', z') system. For each cell-centered position (x', y', z'), we compute a source position (x, y, z) from the coordinate transformation:

$$\begin{pmatrix} x \\ y \\ z \end{pmatrix} = \begin{pmatrix} 1 & 0 & 0 \\ 0 & \cos i & \sin i \\ 0 & -\sin i & \cos i \end{pmatrix} \begin{pmatrix} x' \\ y' \\ z' \end{pmatrix}. \quad (4)$$

In turn, the Cartesian coordinate positions (x, y, z) are related to source cylindrical coordinates (ϖ, φ, z) by $x = \varpi \cos \varphi$, $y = \varpi \sin \varphi$, and $z = z$.

Although we invoke pulsed shock waves to heat and partially ionize the X-wind outflow, we suppose that the shock waves are relatively weak and do not greatly perturb the overall kinematics and density structure imprinted on the flow by the basic magnetohydrodyamics of the X-wind mechanism. In the

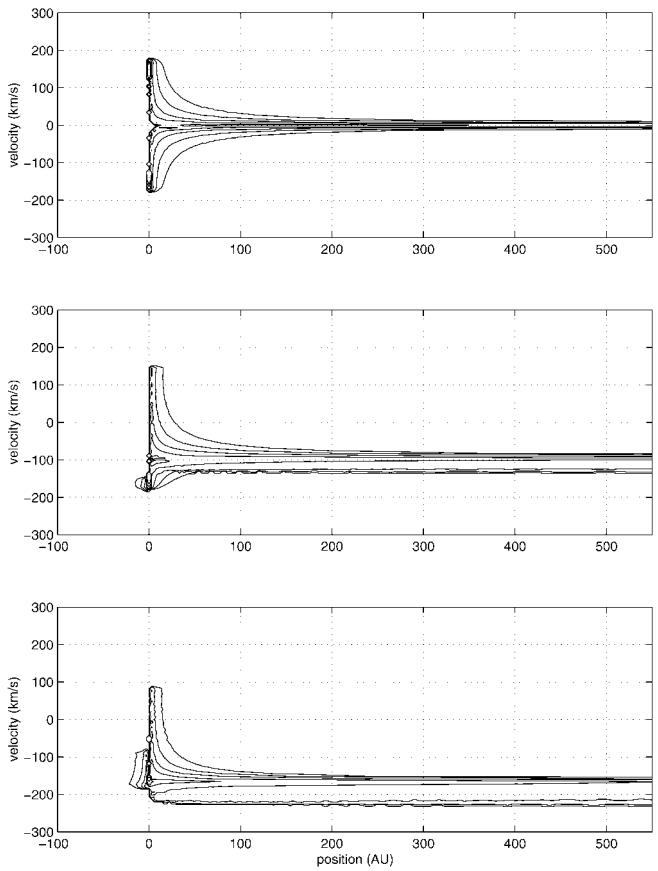

FIG. 3.—Position-velocity diagrams, with y' as the horizontal axis and $v_\parallel$ as the vertical axis, for [S II] λ6731 emission when the synthetic spectrum is taken with a long slit placed along the length of the jet but displaced laterally by $1.5R_X$ with respect to its central axis. The different figures correspond to inclination angles $i = 90°$ (*top*), 60° (*middle*), and 30° (*bottom*). Each contour level for I_λ differs by $10^{1/2}$ from the adjacent level. An integral across the velocity axis for fixed y' in the top panel would give the integrated intensity I displayed in Fig. 2 at the corresponding spatial position ($x' = 1.5R_X \approx 0.08$ AU, y'). A plot of I_λ vs. velocity $v_\parallel$ for fixed y' would yield a line profile for the corresponding spatial position. The line profiles are generally quite asymmetrical, although the contribution from the innermost parts of the jet that gives rise to the highest negative velocities is a little noisy because of inaccuracies of numerical integration near the hollow core.

steady state and axisymmetric approximation, all fluid variables depend only on ϖ and z. Figure 1 shows streamlines and isodensity contours in the meridional plane for a particular dimensionless example computed according to the approximate method of Shang & Shu (1998) that simplifies the exact procedure of Najita & Shu (1994). For the sample calculations of this Letter, we scale the model in Figure 1 according to the following choice of parameters: wind mass-loss rate, $\dot{M}_w = 5 \times 10^{-7}\ M_\odot\ \mathrm{yr}^{-1}$; radius of the inner edge of the gas disk, $R_X = 12\ R_\odot$; and Keplerian velocity of the disk at the base of the X-wind flow, $R_X\Omega_X = 92\ \mathrm{km\ s}^{-1}$.

In the optically thin limit, the line radiation registered at any wavelength within the total line width $\Delta\lambda$ in the pixel centered on (x', y') is

$$\frac{D^2}{\Delta x'\Delta y'}\int_{\Delta\lambda} F'_\lambda d\lambda = \frac{\bar{N}_u A_{ul} E_{ul}}{4\pi}, \qquad (5)$$

where $\bar{N}_u$ is the average column density of atoms in the upper state within pixel $\Delta x'\Delta y'$,

$$\bar{N}_u \equiv \frac{1}{\Delta x'\Delta y'}\int_{\Delta x'} dx' \int_{\Delta y'} dy' \int_{z'>y'\tan i} n_u dz'. \qquad (6)$$

The quantities on either side of equation (5) have the units ergs $\mathrm{s}^{-1}\ \mathrm{cm}^{-2}\ \mathrm{sr}^{-1}$ and, except for the effects of dust extinction, can be compared directly with observed measurements of surface brightness, independent of the distance D to the source. To derive equation (5), we have assumed that an optically thick disk allows the observer to view only the jet for $z > 0$, i.e., $z' > y' \tan i$, with radiation from a volume element $\Delta V'$ contributing line emission centered on the wavelength $\lambda = \lambda_{ul}(1 + v_\parallel/c)$, where λ_{ul} is the rest wavelength of the spectral line. In the above, $v_\parallel = -\boldsymbol{v}\cdot\nabla z'$, where $\boldsymbol{v}$ is the fluid velocity of the jet measured in an inertial frame, with components $(v_\varpi, v_\varphi, v_z)$ in cylindrical coordinates, and $\nabla z'$ is the unit vector of the observer's direction. From the matrix inverse of equation (4), the line-of-sight velocity attributed by the observer to the center of the volume element can now be obtained as

$$v_\parallel = -(v_\varpi \sin i \sin\varphi + v_\varphi \sin i \cos\varphi + v_z \cos i). \qquad (7)$$

Except for the central volume element, the spread of wavelengths in $\Delta V'$ is small enough that all the radiation from that cell can be thrown into a single velocity bin for an appropriately divided wavelength range. In such cells we replace equation (6) by $N_u = \sum_{z'} n_u \Delta z'$, with n_u calculated at (x', y', z'). The central volume element has too much structure to be well represented by a cell of size equal to those farther out, and it is given a special subdivision to resolve its velocity features.

4. RESULTS

Figure 2 (Plate L8) shows edge-on views of the fiducial X-wind model in [S II] λ6731 and [O I] λ6300 emission. Because the emission arises preferentially in regions with density higher than critical, the surface brightness distributions take on the appearance of a highly collimated jet, despite the fact that the streamlines in Figure 1 collimate logarithmically slowly in reality (see SNOS). Because of the higher critical density of the [O I] λ6300 transition, the [O I] image is brighter but more centrally concentrated than the [S II] image. In real systems, the extinction by dust entrained in the flow, a depletion of oxygen atoms onto molecules or grains, or a decreasing electron fraction farther from the central source may cut down the brightness contrast of [O I] to [S II]. Real jets also have a knottier appearance than our model, and future modeling efforts should include estimates for the time-dependent heating and ionization effects associated with jets that pulse.

Notice at high enough spatial resolution that the images in Figure 2 have a slight depression along the central axis of the jet (a drop in surface brightness $\sim 2/\pi$). The depression in projected light arises because the physical X-wind flow is hollow at its core (SNOS). Detection of this hollow core in the nearest protostellar jets requires angular resolution about 5 times greater than that available with the *Hubble Space Telescope*. Such a difficult task would nevertheless be quite rewarding because it would establish whether stellar field lines really need to be opened in order to magnetocentrifugally drive YSO jets. Because of the low contrast, an optical interferometer with a nearly filled aperture like the University of Arizona's large binocular telescope is probably the best short-term hope for a test of this prediction.

Figure 3 shows synthetic long-slit spectrograms of the [S II] λ6731 jet in Figure 2 when that jet has inclination angles $i = 90^\circ$, 60°, and 30°. The position-velocity diagrams look similar in the [S II] λ6716 and [O I] lines. To avoid computational problems associated with very dense gas in the main acceleration region of the flow, the theoretical slit has been placed at an offset of $1.5R_X$ from the central axis. Near the central position of real sources, [O I] λ6300/λ6364 line profiles often show a separate low-velocity, slightly blueshifted, feature (Edwards et al. 1987). Kwan & Tademaru (1988) and others have interpreted this separate feature in terms of the coexistence of a slow (disk) wind and a fast (X-) wind. Without higher resolution calculations of the very central regions including better input physics and chemistry, we are unable to comment on the necessity of this interpretation.

In Figure 3, the line profiles are very broad at the base of the jet, containing both large positive and large negative values of $v_\parallel$. The effect arises because the streamlines at the base of the jet in Figure 1 fan out in a variety of directions, toward and away from the observer, despite the fact that the image of the jet in Figure 2 looks strongly one-dimensional. At the base of YSO flows, therefore, the visual appearance of jets is somewhat of an *optical illusion*.

As we go up the jet along the length of the slit, the [S II] λ6731 line profile narrows until it straddles the (negative) velocity expected naively for a highly collimated flow inclined toward the observer and traveling at a terminal velocity v_z varying on different streamlines from 180 to 270 km s^{-1}. Because of projection effects, there is an apparent deceleration of the envelope of the line profiles at high negative velocities as one samples the emission along the length of the jet. The apparent deceleration at the base does *not* represent a mixing of high- and low-velocity material (cf. Solf & Böhm 1993; Lavalley et al. 1997; Hirth, Mundt, & Solf 1997). A second, slow, disk wind may indeed be present in the actual sources, but the broad, high-velocity features seen in Figure 3 at the base of the flow arise purely from line-of-sight effects of a gradually collimating, wide-angle, X-wind.

Given the simplicity of the underlying assumptions, we regard the qualitative agreement between the synthetic long-slit spectra computed in Figure 3 versus similar spectra seen in many real sources (Solf & Böhm 1993; Bacciotti, Chiuderi, & Oliva 1995; Bacciotti, Hirth, & Natta 1996; Lavalley et al. 1997; Hirth et al. 1997) as providing strong support for X-wind theory. It would be interesting to pursue more quantitative source-by-source comparisons, in several spectral lines and in the free-free radio continuum (Rodriguez 1997).

This work is supported in part by grants from the NASA Origins of Solar Systems Program and from the National Science Foundation. We thank Gibor Basri, Suzan Edwards, James Graham, and Bo Reipurth for illuminating discussions.

REFERENCES

Bacciotti, F., Chiuderi, C., & Oliva, E. 1995, A&A, 296, 185
Bacciotti, F., Hirth, G. A., & Natta, A. 1996, A&A, 310, 309
Bachiller, R. 1996, ARA&A, 34, 111
Bally, J., & Lada, C. J. 1983, ApJ, 265, 824
Bok, B. J. 1978, PASP, 90, 489
Cabrit, S., Raga, A. C., & Gueth, F. 1997, in IAU Symp. 182, Herbig-Haro Flows and the Birth of Low Mass Stars, ed. B. Reipurth & C. Bertout (Dordrecht: Kluwer), 163
Chernin, L., & Masson, C. 1995, ApJ, 455, 182
Cudworth, K. M., & Herbig, G. H. 1979, AJ, 84, 548
Edwards, S., Cabrit, S., Strom, S., Heyer, I., Strom, K., & Anderson, E. 1987, ApJ, 321, 473
Haro, G. 1950, AJ, 55, 72
Herbig, G. H. 1950, ApJ, 111, 11
Hirth, G. A., Mundt, R., & Solf, J. 1997, A&AS, 126, 437
Kwan, J., & Tademaru, E. 1988, ApJ, 332, L41
Lavalley, C., Cabrit, S. Dougados, C., Ferruit, & Bacon, R. 1997, A&A, 327, 671
Li, Z. Y., & Shu, F. H. 1996, ApJ, 472, 211
Masson, C., & Chernin, L. 1992, ApJ, 387, L47
Mendoza, C. 1983, in IAU Symp. 103, Planetary Nebulae, ed. D. R. Flower (Dordrecht: Reidel), 143
Mundt, R., & Fried, J. W. 1983, ApJ, 274, L83
Myers, P. C., Fuller, G. A., Goodman, A. A., & Benson, P. J. 1991, ApJ, 376, 561
Najita, J. R., & Shu, F. H. 1994, ApJ, 429, 808
Raga, A. C. 1995, Rev. Mexicana Astron. Astrofis. Ser. Conf. 1, 103
Reipurth, B., & Heathcote, S. 1991, A&A, 246, 511
Rodriguez, L. F. 1997, in IAU Symp. 182, Herbig-Haro Flows and the Birth of Low Mass Stars, ed. B. Reipurth & C. Bertout (Dordrecht: Kluwer), 83
Rodriguez, L. F., Ho, P. T. P., & Moran, J. M. 1980, ApJ, 240, L149
Shang, H., & Shu, F. H. 1998, in preparation
Shu, F. H., Najita, J., Ostriker, E., & Shang, H. 1995, ApJ, 455, L155 (SNOS)
Shu, F., Najita, J., Ostriker, E., Wilkin, F., Ruden, S., & Lizano, S. 1994, ApJ, 429, 781
Shu, F. H., Ruden, S. P., Lada, C. J., & Lizano, S. 1991, ApJ, 370, L31 (SRLL)
Shu, F. H., & Shang, H. 1997, in IAU Symp. 182, Herbig-Haro Flows and the Birth of Low Mass Stars, ed. B. Reipurth & C. Bertout (Dordrecht: Kluwer), 225
Shu, F. H., Shang, H., Glassgold, A. E., & Lee, T. 1997, Science, 277, 1475
Snell, R. L., Loren, R. B., & Plambeck, R. L. 1980, ApJ, 239, L17
Solf, J., & Böhm, K.-H. 1993, ApJ, 410, L31
Welch, W. J., Vogel, S. N., Plambeck, R. L., Wright, M. C. H., & Bieging, J. H. 1985, Science, 228, 1329

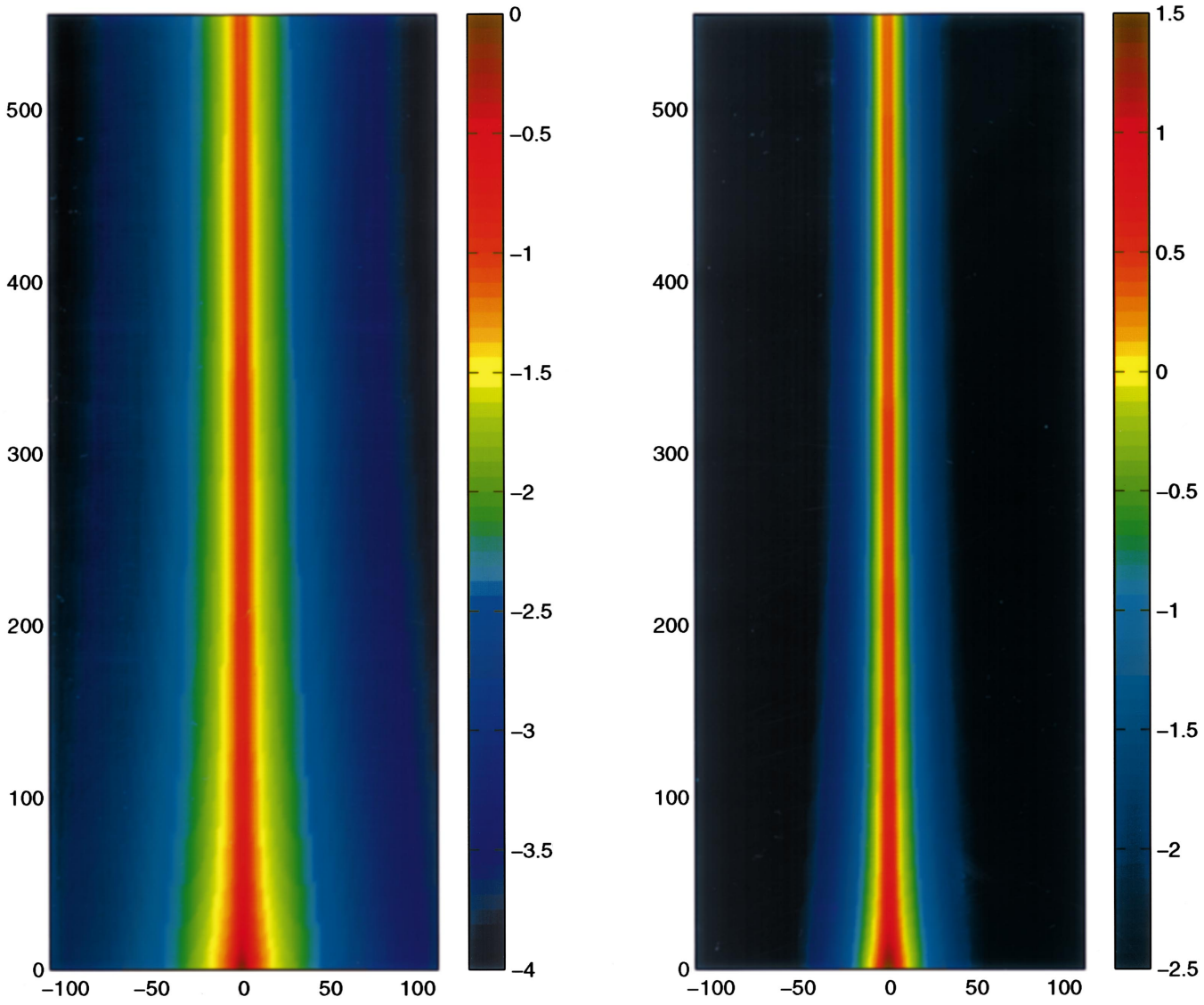

FIG. 2.—Synthetic images of [S II] λ6731 (*left*) and [O I] λ6300 emission (*right*). The units of length are AU, and the color code is for $\log_{10} I$, where I is the specific intensity in the line in units of ergs s^{-1} cm^{-2} sr^{-1}. For electron densities much larger than the critical density in the X-wind, eq. (5) yields $I \propto 1/x'$ (except for impact parameters x' within the hollow core), while for electron densities much smaller than the critical density, the same equation gives $I \propto 1/x'^3$. Thus, the effective width of the jet is defined in practice by the point at which n_e equals the critical value, which occurs closer to the jet axis for [O I] than for [S II].

SHANG, SHU, & GLASSGOLD (see 493, L93)